Applied Physics Express

LETTER

Anisotropic electrical properties of NiO_x/β-Ga_2O_3 *p*-*n* heterojunctions on $(\bar{2}01)$, (001), and (010) crystal orientations

Applied Physics Express **16**, 094002 (2023) **LETTER**
https://doi.org/**10.35848/1882-0786/acf8ad**

Anisotropic electrical properties of NiO_x/β-Ga_2O_3 *p-n* heterojunctions on $(\bar{2}01)$, (001), and (010) crystal orientations

Dinusha Herath Mudiyanselage[1], Ramandeep Mandia[2], Dawei Wang[1], Jayashree Adivarahan[1], Ziyi He[1], Kai Fu[3], Yuji Zhao[4], Martha R. McCartney[5], David J. Smith[5], and Houqiang Fu[1*]

[1]*School of Electrical, Computer, and Energy Engineering, Arizona State University, Tempe, AZ 85287, United States of America*
[2]*School of Engineering for Matter, Transport and Energy, Arizona State University, Tempe, AZ 85287, United States of America*
[3]*Department of Electrical and Computer Engineering, The University of Utah, Salt Lake City, UT 84112, United States of America*
[4]*Department of Electrical and Computer Engineering, Rice University, Houston, TX 77005, United States of America*
[5]*Department of Physics, Arizona State University, Tempe, AZ 85287, United States of America*

[*]E-mail: houqiang@asu.edu

Received August 1, 2023; revised September 2, 2023; accepted September 11, 2023; published online September 25, 2023

NiO_x/β-Ga_2O_3 *p-n* heterojunctions fabricated on $(\bar{2}01)$, (001), and (010) β-Ga_2O_3 substrates show distinctly anisotropic electrical properties. All three devices exhibited excellent rectification $\geqslant 10^9$, and turn-on voltages >2.0 V. The (010) device showed very different turn-on voltage, specific on-resistance, and reverse recovery time compared with $(\bar{2}01)$ and (001) devices. Moreover, it is calculated that the interface trap state densities for $(\bar{2}01)$, (001), and (010) plane devices are 4.3×10^{10}, 7.4×10^{10}, and 1.6×10^{11} $eV^{-1}cm^{-2}$, respectively. These differences in the NiO_x/β-Ga_2O_3 heterojunctions are attributed to the different atomic configurations, the density of dangling bonds, and interface trap state densities.

There has been substantial recent interest in ultra-wide bandgap (UWBG) semiconductors, such as gallium oxide (β-Ga_2O_3),[1)] aluminum nitride,[2)] diamond,[3)] and boron nitride[4)] for power electronics due to their large bandgaps and high critical field. These properties can result in higher operating voltages, larger currents, increased efficiencies, and smaller device footprint compared to devices based on traditional semiconductors such as silicon and wide bandgap semiconductors such as silicon carbide and gallium nitride.[5)] As an emerging UWBG material, β-Ga_2O_3 has attracted much attention for electronic and photonic device applications.[1)] However, a significant challenge for β-Ga_2O_3 is its lack of *p*-type conductivity. Theoretical predictions indicate a difficulty in obtaining holes due to the high activation energy (>1 eV) of acceptors for β-Ga_2O_3.[6)] Moreover, due to the flat valence band maximum, the heavy hole effective mass leads to low hole mobility[7)] while holes tend to be localized in β-Ga_2O_3 as polarons due to lattice distortion.[8)] Thus, most reported β-Ga_2O_3 devices, such as field effect transistors[9)] and Schottky barrier diodes,[10)] are unipolar. The demonstration of *p-n* junctions in β-Ga_2O_3 is critical for the development of bipolar devices and advanced Ga_2O_3-based electronic devices.

Recently, *p*-NiO_x has emerged as a popular choice for the formation of β-Ga_2O_3 *p-n* heterojunctions due to its easy deposition and extensive use as a hole contact in high-efficiency solar cells.[11,12)] Kokubun et al.[13)] demonstrated the first NiO_x/β-Ga_2O_3 *p-n* heterojunction with Li-doped NiO_x epitaxial layer. Several NiO_x/β-Ga_2O_3 heterojunctions, including *p-n* diodes[14–16)] and junction barrier Schottky diodes[17–19)] have been demonstrated with excellent electrical characteristics, such as low on-resistance, high on/off ratio, and large reverse blocking voltage. Moreover, NiO_x/β-Ga_2O_3 heterojunctions are versatile with a wide range of applications, including edge terminations in β-Ga_2O_3 power diodes[20)] and all-oxide-based UV photodetectors.[21)]

The low crystal symmetry of monoclinic β-Ga_2O_3 results in highly anisotropic material with a direct impact on several key physical and electronic properties, such as dielectric constant,[22)] thermal conductivity,[23)] and electron mobility[24)] which are different along different crystallographic directions. This anisotropy poses challenges for device fabrication and results in discrepancies in device performance. Fu et al.[24)] compared Schottky contacts on $(\bar{2}01)$ and (010) β-Ga_2O_3 planes and observed that the (010) orientation had higher barrier height and lower reverse leakage. Sasaki et al.[25)] reported that the rate of epitaxial growth on the (100) plane was slower compared to the (010) plane due to the low adhesion energy on (100) terraces. Jang et al.[26)] found that the etch rate and ability to form Ohmic contacts on $(\bar{2}01)$ plane was higher compared to (010) plane owing to the higher density of oxygen dangling bonds. However, the anisotropic properties of the widely used NiO_x/β-Ga_2O_3 heterojunctions are not well understood. In this work, a systematic comparative analysis of NiO_x/β-Ga_2O_3 *p-n* heterojunctions with $(\bar{2}01)$, (001), and (010) substrate orientations has been carried out. Temperature-dependent electrical measurements, reverse recovery characteristics, and capacitance–frequency (*C–f*) measurements, were performed to provide a better understanding of the anisotropic nature of NiO_x/β-Ga_2O_3 *p-n* heterojunctions.

Figure 1(a) shows the crystal structure of β-Ga_2O_3 and the corresponding planes used as substrates for this study. These β-Ga_2O_3 planes are widely used for β-Ga_2O_3 devices. Previous literature has shown clear differences between $(\bar{2}01)$ [or (001)] and (010) plane dangling bond densities, which were calculated to be 2.68×10^{15} [or 2.69×10^{15}] and 1.74×10^{15} cm^{-2}, respectively.[27)] Edge-defined film-fed grown $(\bar{2}01)$, (001), and (010) β-Ga_2O_3 substrates from Novel Crystal Technology were used for this study.[28)] The substrates had similar *n*-type [Sn] doping concentrations of $\sim 5 \times 10^{18}$ cm^{-3}, similar thickness, and good crystalline quality, as verified by XRD measurements. To prepare the substrates, a standard cleaning procedure was implemented, which included cleaning with acetone, isopropyl alcohol, and deionized water, aided by sonication. The back contacts of Ti/Au (20/130 nm) were deposited using electron beam (E-beam) evaporation. followed by rapid thermal annealing at 500 °C in an N_2 environment. All back contacts showed very low contact resistance of <0.01 $m\Omega cm^2$. Standard

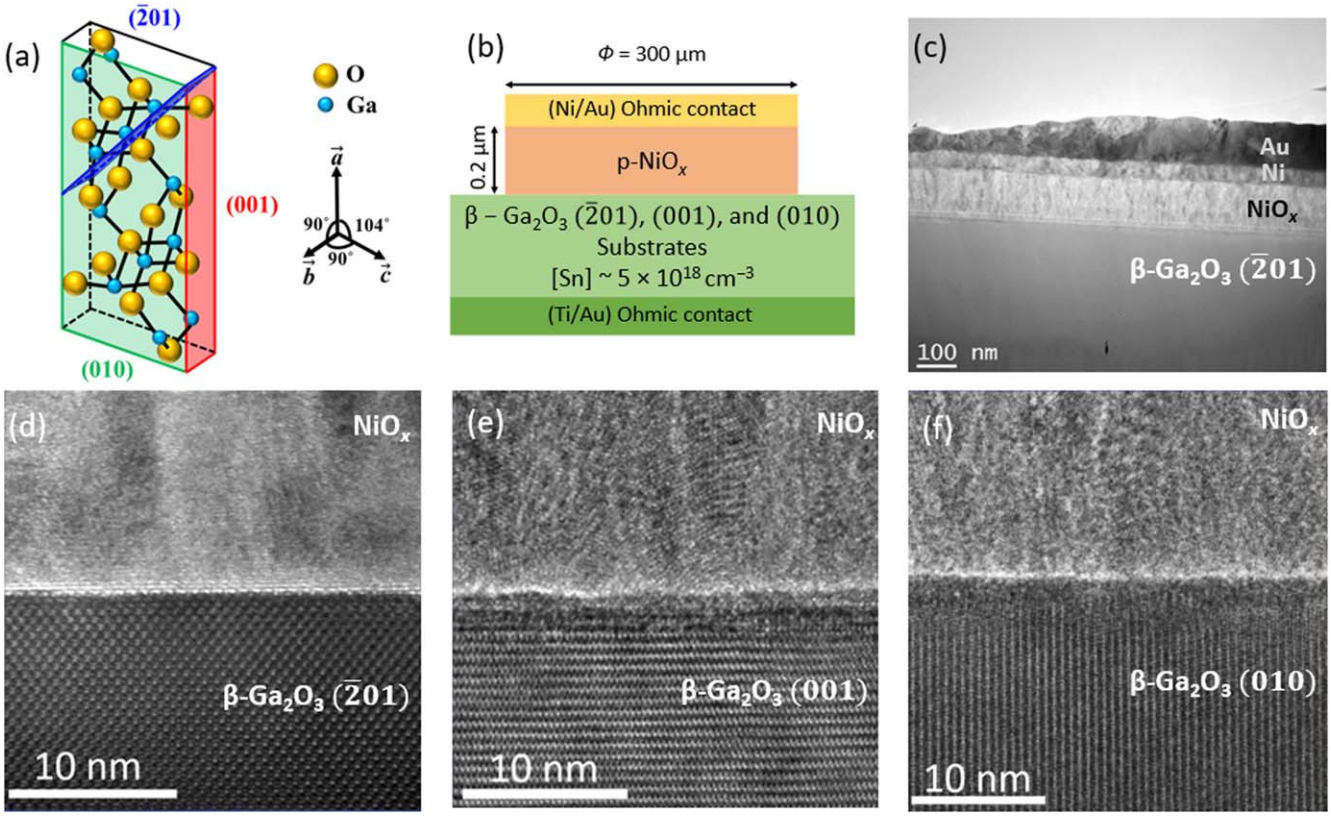

Fig. 1. (a) Monoclinic crystal structure of β-Ga_2O_3 with crystal planes of ($\bar{2}$01), (001), and (010) labeled. (b) Schematic of fabricated NiO_x/β-Ga_2O_3 *p-n* heterojunctions. (c) TEM image of the interfaces of NiO_x/β-Ga_2O_3 heterojunctions fabricated on ($\bar{2}$01) plane. HRTEM images of the NiO_x/β-Ga_2O_3 interface of (d) ($\bar{2}$01), (e) (001), and (f) (010) devices.

photolithography was then performed to define circular patterns for the deposition of NiO_x and the anode (diameter of 300 μm). 200 nm NiO_x and the anode Ni/Au (20/130 nm) were deposited using E-beam evaporation, followed by a lift-off process. The fabricated device structure and device dimensions are shown in Fig. 1(b). The anode, cathode, and NiO_x layers were deposited simultaneously for all samples to avoid any inconsistencies in fabrication. All NiO_x layers were highly doped with a similar hole density of $>2 \times 18\,cm^{-3}$, and the Ohmic contacts to NiO_x layers had a similar contact resistance of $\sim$0.3 mΩcm^2. After device fabrication, all samples were annealed at 350 °C in N_2 ambient for 1 min. This annealing step was expected to improve the device performance by forming an Ohmic contact between the Ni/NiO_x interface and reducing the number of interface states at the NiO_x/β-Ga_2O_3 heterojunction.[29)]

Electrical characterization was conducted using a probe station equipped with a controllable thermal chuck, Keithley 4200-SCS parameter analyzer, and ultra-fast pulse measurement units. Cross-sectional transmission electron microscope (XTEM) images were taken for all samples. The TEM samples were prepared using a Thermo Fisher Helios 5UX Dualbeam system with final thinning in a Gatan precision ion-polishing system. The milling started with a Ga-focused ion beam at 30 keV, followed by thinning at 5 and 2 keV, and subsequent Ar-ion thinning at 2 and 1 keV. Devices with ($\bar{2}$01), (001), and (010) β-Ga_2O_3 substrate normals were imaged along their respective [010], [100] and [001] zone axes. High-resolution TEM (HRTEM) images were taken using a Philips CM 200 operated at 200 kV and an image-corrected FEI Titan 80–300 operated at 300 kV. Figure 1(c) shows an XTEM image of the full diode structure consisting of the top electrode (Au, Ni), NiO_x, and β-Ga_2O_3 substrate. Figures 1(d)–1(f) show HRTEM images of the NiO_x/β-Ga_2O_3 interface for samples grown on ($\bar{2}$01), (001) and (010) substrates, respectively. The polycrystalline nature of NiO_x layers was evident in HRTEM images, and abrupt NiO_x/β-Ga_2O_3 interfaces were clearly visible.

Figure 2(a) shows *I–V* curves for the three NiO_x/β-Ga_2O_3 *p-n* diodes, where the turn-on voltages were 2.09, 2.22, and 2.50 V for ($\bar{2}$01), (001), and (010) substrates, respectively. Devices on ($\bar{2}$01) and (001) planes had excellent rectification ratios of $\sim 10^{10}$ at ±3.75 V. However, (010) devices showed a smaller on/off ratio of about $\sim 10^9$ at ±3.75 V. Furthermore, devices on ($\bar{2}$01) and (001) planes exhibited specific on-resistances of 2.92 and 1.55 mΩcm^2, while the (010) device showed a specific on-resistance of 6.50 mΩcm^2. Ideality factors were 1.95, 2.03, and 2.13 for ($\bar{2}$01), (001), and (010) planes, respectively. These large ideality factors indicate that the current recombination in the heterojunction is dominant compared to diffusion currents.

The *C–V* measurements were performed at a frequency of 100 kHz [Fig. 3(a)], and the devices showed built-in potentials of 2.72, 2.74, and 2.63 V on ($\bar{2}$01), (001), and (010) devices, respectively [Fig. 3(b)]. The built-in voltages were comparable in all three devices since there is no current transport through the devices in *C–V* measurements. The built-in voltages determined by *I–V* and *C–V* measurements showed some discrepancies. In general, *C–V* measurements are mainly affected by the doping concentration of NiO_x and β-Ga_2O_3, as well as the charges from the interface states. However, they do not provide information about the current

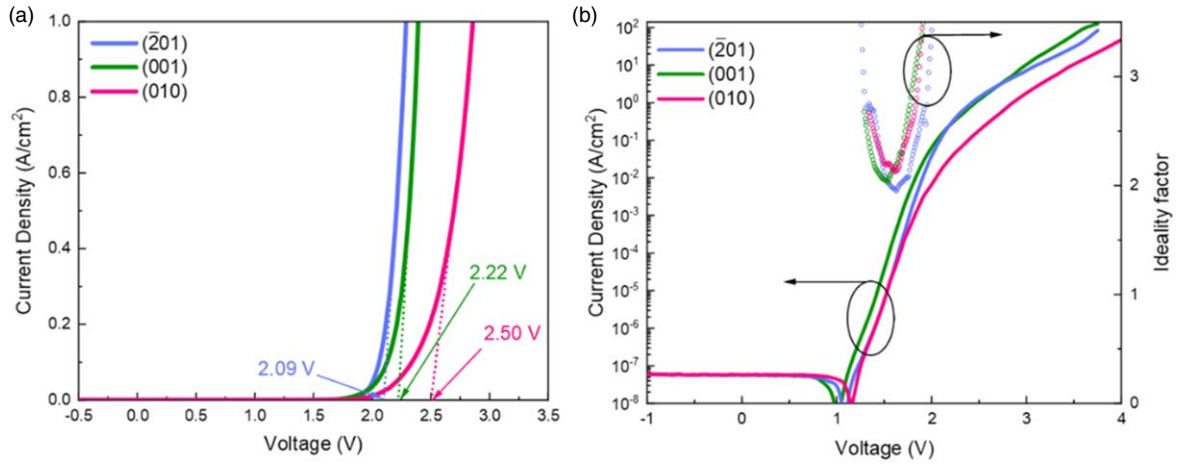

Fig. 2. *I–V* characteristics of NiO_x/β-Ga_2O_3 *p-n* heterojunctions on three crystallographic orientations: (a) linear scale and (b) semi-log scale.

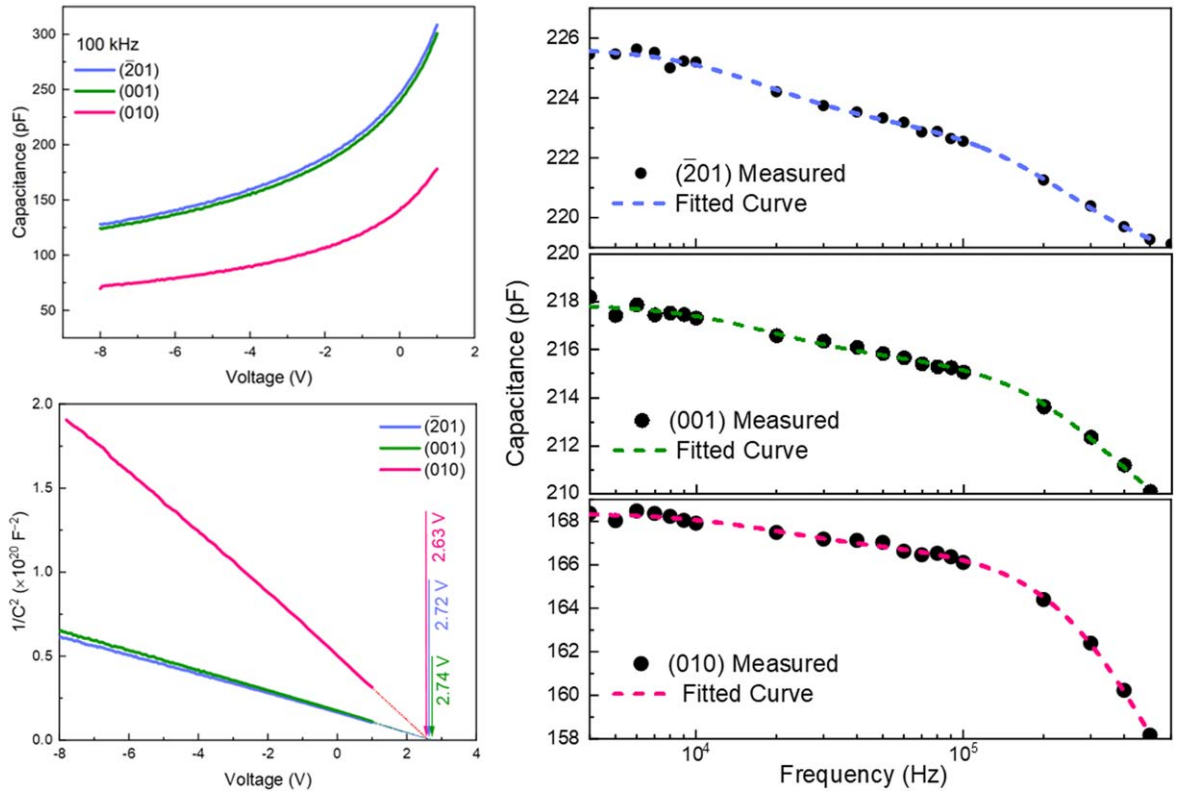

Fig. 3. (a) *C–V* measurements, and (b) $1/C^2$–*V* plots of NiO_x/β-Ga_2O_3 *p-n* heterojunctions for three crystallographic orientations. The *C–f* characteristics with corresponding fitting curves for devices on (c) ($\bar{2}$01), (d) (001), and (e) (010) planes.

conduction through the interface. Conversely, extraction of built-in voltage through *I–V* measurements is influenced by the crystal anisotropy and interface states. The effective carrier concentration $(N_d - N_a + N_t)$[30] calculated from the *C–V* measurements was 4.7×10^{18}, 4.5×10^{18}, $1.6 \times 10^{18}\,cm^{-3}$ for ($\bar{2}$01), (001), and (010) devices, respectively, where N_d is the ionized donor concentration, N_a is the ionized acceptor concentration, and N_t is the equivalent charge concentration of traps. Since the β-Ga_2O_3 and NiO_x film in the three samples had similar carrier concentrations, the observed variation in the effective carrier concentrations is likely related to the different NiO_x/β-Ga_2O_3 heterojunction interfaces caused by the crystal anisotropy, which is verified by C–*f* measurements.

Figures 3(c)–3(e) show *C–f* measurements for the devices on ($\bar{2}$01), (001), and (010) substrates to evaluate the interface trap state density (D_{it}). The *C–f* measurements are fitted using the equations below, assuming the interface states are distributed in two energy levels.[31,32]

$$C = C_{sc} + \frac{C_{it-1}}{(1 + 2\pi f\tau_1)^2} + \frac{C_{it-2}}{(1 + 2\pi f\tau_2)^2} \quad (1)$$

$$D_{it} = C_{it}/q^2A \quad (2)$$

where C_{sc} is the capacitance of the space charge region, and $C_{it-1}(C_{it-2})$ is the capacitance of the first state (second state) with their corresponding relaxation time τ_1 (τ_2). C_{it-1} represents an energy level that corresponds to interface states closer to the

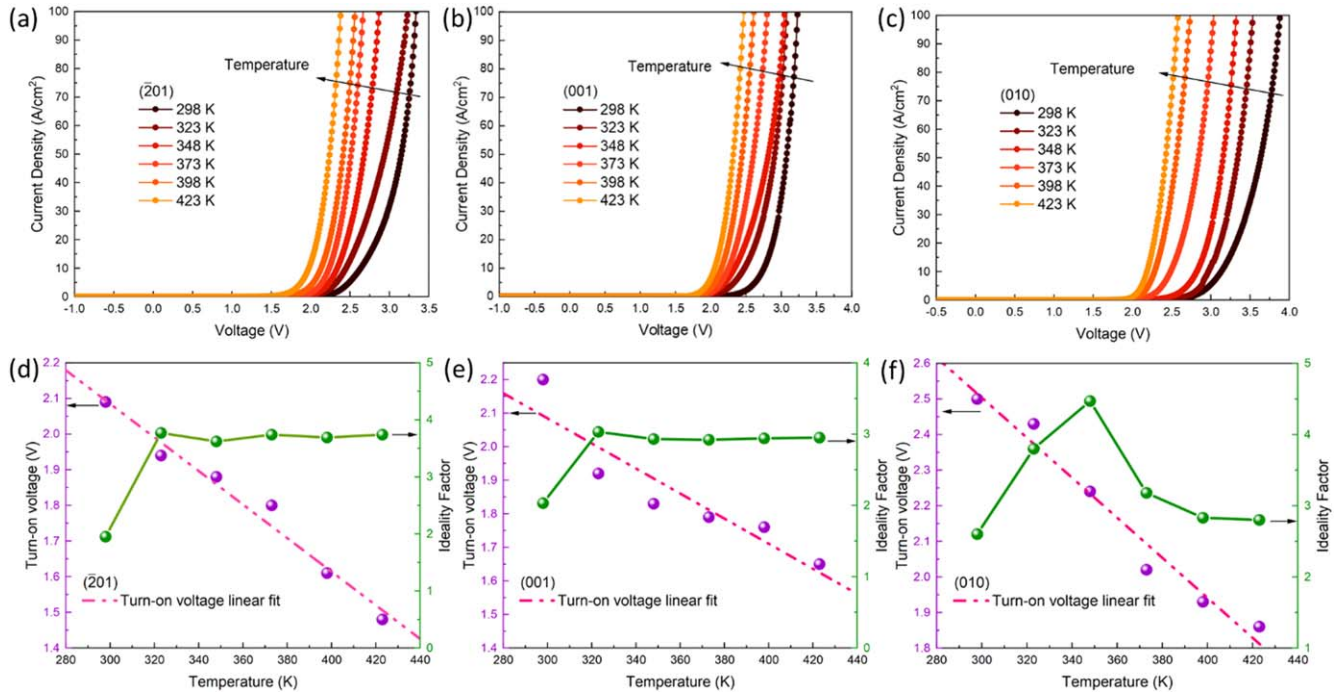

Fig. 4. Temperature-dependent *I–V* curves for the devices on (a) ($\bar{2}01$), (b) (001), and (c) (010). Variation of turn-on voltage and ideality factor of corresponding *I–V* curves are shown in (d), (e), and (f).

Table I. Interface state parameters extracted from *C–f* curve fitting.

Orientation	C_{it-1} (F)	C_{it-2} (F)	τ_1 (s)	τ_2 (s)	D_{it-1} ($eV^{-1}cm^{-2}$)	D_{it-2} ($eV^{-1}cm^{-2}$)
($\bar{2}01$)	4.80×10^{-12}	2.50×10^{-12}	0.64×10^{-6}	8.69×10^{-6}	4.3×10^{10}	2.2×10^{10}
(001)	8.36×10^{-12}	2.27×10^{-12}	0.43×10^{-6}	8.57×10^{-6}	7.4×10^{10}	2.0×10^{10}
(010)	1.79×10^{-11}	1.62×10^{-12}	0.34×10^{-6}	8.02×10^{-6}	1.6×10^{11}	1.4×10^{10}

conduction band with a smaller relaxation time, and C_{it-2} represents a deep energy level with a considerably larger relaxation time. A similar C_{it-2} of $\sim 2 \times 10^{-12}$ F was observed with a relaxation time of about ~ 8 μs for all devices. This may represent deep-level states (e.g., vacancies) with relaxation time much larger than the interface states. However, C_{it-1} varied significantly for devices on different crystal orientations. The relaxation time for C_{it-1} was 0.64, 0.43, and 0.34 μs for (201), (001), and (010) devices, respectively, which are consistent with previous reports.[31,32] C_{it-1} changed with crystal orientation, while C_{it-2} remained relatively constant. It should be noted that the exact nature of the defect states in NiO_x/β-Ga_2O_3 diodes is still unclear and demands further investigation. The extracted interface trap densities (D_{it-1}) from C_{it-1} were 4.3×10^{10}, 7.4×10^{10}, and 1.6×10^{11} $eV^{-1}cm^{-2}$ for ($\bar{2}01$), (001), and (010) devices, respectively.[29,31,32] The interface states derived from C_{it-1} are much closer to the conduction band, and thus may play an important role in the device performance. Table I summarizes all the parameters extracted through *C–f* curve fitting.

The differences in electrical properties of NiO_x/β-Ga_2O_3 *p-n* heterojunctions can be attributed to several factors. First, the difference in interface states may be significantly promoted by the density of dangling bonds. If the number of dangling bonds is high, then the adhesion of the NiO_x layer is promoted, exhibiting fewer interface states. Due to the higher dangling bond density in ($\bar{2}01$) and (001) plane, it is easier to form better-quality NiO_x/β-Ga_2O_3 heterojunction with high surface energy.[27] This is analogous to the fact that forming Ohmic contacts on ($\bar{2}01$) and (001) planes is easier than on (010) plane.[26] Second, different doping concentrations can be induced in the heterojunction due to interface states. The interface states can have a big impact on net charge density. It is likely that there are lower compensating trap states in ($\bar{2}01$) and (001) NiO_x/β-Ga_2O_3 *p-n* heterojunctions as indicated by the *C–f* measurement, contributing larger net charge densities. This is further evidenced by the different gradients in the $1/C^2$–*V* plot. The observed differences are primarily influenced by the presence of interface states, considering three NiO_x and β-Ga_2O_3 in the three samples had similar carrier concentrations. As discussed later, a difference in reverse recovery time (t_{rr}) of the devices was observed, indicating that carrier recombination on different planes is affected by the crystal anisotropy.

The temperature-dependent forward characteristics of three NiO_x/β-Ga_2O_3 *p-n* diodes are presented in Figs. 4(a)–4(c). The observed temperature-dependent behavior was stable and reproducible, and the initial *I–V* curves were retained even after heating and cooling down, indicating excellent thermal stability of the heterojunction.[16,29] The device ideality factor and turn-on voltage were extracted as a function of temperature, as shown in Figs. 4(d)–4(f). The turn-on voltage decreased linearly with the temperature, which can be attributed to the reduction of depletion width facilitating diffusion of holes.[33] The ideality factor varied between 1.95–3.77, 2.03–2.95, and 2.13–4.47 in ($\bar{2}01$), (001), and

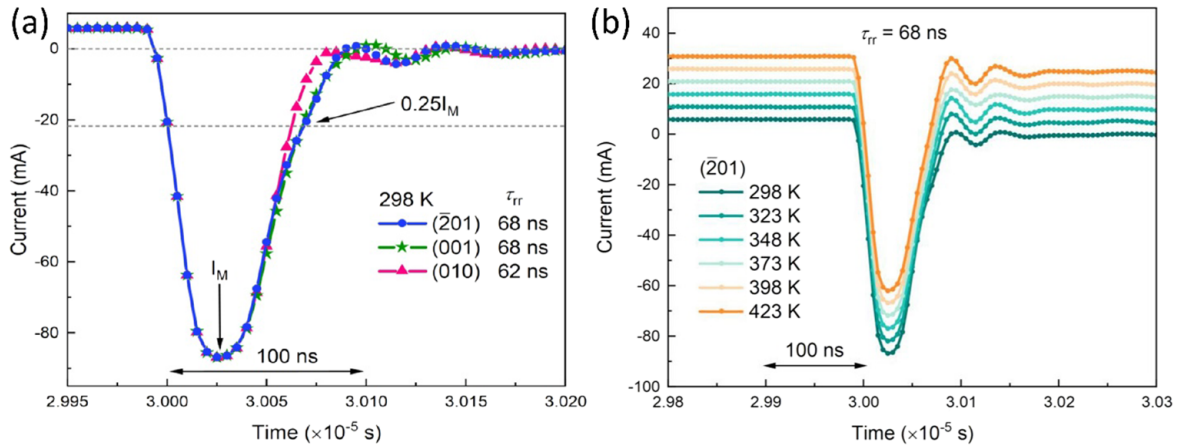

Fig 5. (a) Reverse recovery of NiO_x/β-Ga_2O_3 *p-n* heterojunctions on three crystallographic orientations. (b) Temperature-dependent reverse recovery of *p-n* diodes on (2̄01) plane.

Table II. Electrical properties of the NiO_x/β-Ga_2O_3 *p-n* diode heterojunctions grown on (2̄01), (001), and (010) substrates.

Orientation	$V_{on}(I–V)$ (V)	$V_{bi}(C–V)$ (V)	$R_{sp\text{-}on}$(mΩcm^2)	on/off ratio	η	t_{rr} (ns)	D_{it} (eV^{-1}cm^{-2})
(2̄01)	2.09	2.74	2.92	10^{10}	1.95	68	4.3×10^{10}
(001)	2.22	2.72	1.55	10^{10}	2.03	68	7.4×10^{10}
(010)	2.50	2.63	6.50	10^{9}	2.13	62	1.6×10^{11}

(010) devices, respectively. This behavior of turn-on voltage and ideality factor is consistent with previous reports.[29,33] The ideality factor of (2̄01) and (001) devices remained almost constant under high temperatures. However, the ideality factor in (010) devices first increased and then decreased. This behavior can be attributed to the fact that there are 10 times more interface trap states in (010) heterojunction compared to (2̄01) and (001) heterojunctions. With increasing temperature, the carrier emission from interface traps is enhanced, affecting the ideality factor.

The t_{rr} of the diode is defined as the time it takes to reach $0.25I_M$ after switching off, where I_M is the maximum current during the reverse recovery period. The t_{rr} of the diodes is affected by several factors, including the doping concentration, the width of the depletion region, crystal anisotropy, and the applied voltage. In this work, all three samples were subject to voltages of ±5 V to observe the reverse recovery of the diode. The (2̄01) and (001) devices had a t_{rr} of 68 ns, while (010) devices took 62 ns to recover [Fig. 5(a)]. The shorter reverse recovery time for (010) is likely due to larger interface defect densities that promote electron/hole recombination with a faster recovery time and mobility variation along different crystal orientations. All devices had a peak current of about 86 mA and showed temperature independence[33] in reverse recovery time, as shown in Fig. 5(b), where the *y*-axis is offset for clarity. This indicates that the junction capacitance and stored charges in the depletion region are independent of temperature. The forward current during the reverse recovery test was ∼6 mA. Additionally, the di/dt of three samples for the reverse recovery characteristics was 3.95 A μs^{-1}, which is comparable to previously reported values.[33] The reverse recovery charge was 4.47, 4.54, and 4.26 nC for (2̄01), (001), and (010) devices, respectively. The different t_{rr} in different crystal orientations indicate carrier recombination is influenced by the interface states. Table II summarizes the device parameters of the three NiO_x/β-Ga_2O_3 *p-n* heterojunctions, where D_{it} of the devices is based on the dominant D_{it-1} values.

In conclusion, NiO_x/β-Ga_2O_3 *p-n* heterojunctions fabricated on (2̄01), (001), and (010) substrates showed considerable differences in electrical properties in terms of turn-on voltages, ideality factor, on-resistance, and reverse recovery time. The (010) device exhibited the highest turn-on voltage of 2.50 V, the highest ideality factor of 2.13, the largest on-resistance of 6.50 mΩcm^2, and the lowest recovery time of 62 ns. The *C–f* measurements indicate an interface trap density of 4.3×10^{10}, 7.4×10^{10}, and 1.6×10^{11} eV^{-1}cm^{-2} for (2̄01), (001), and (010) plane devices, respectively. All devices were fabricated simultaneously and exhibited excellent rectifying behaviors with a high on/off ratio of $\geqslant 10^9$ and high-quality interfaces between NiO_x and β-Ga_2O_3, as confirmed by HRTEM. These differences in device electrical properties are attributed to the different atomic configurations, the density of dangling bonds, and interface trap state densities. These results indicate the anisotropic nature of β-Ga_2O_3 in heterojunction-based *p-n* diodes and should serve as a valuable reference for future development of Ga_2O_3 heterojunction bipolar devices.

Acknowledgments This research is supported as part of ULTRA, an Energy Frontier Research Center funded by the U.S. Department of Energy (DOE), Office of Science, Basic Energy Sciences (BES), under Award # DE-SC0021230. This work is also partially supported by the National Science Foundation (NSF) under Award # 2302696. The authors also acknowledge the use of facilities within the John M. Cowley Center for High Resolution Electron Microscopy at Arizona State University, supported in part by NSF grant ECCS-2025490.

ORCID iDs Dinusha Herath Mudiyanselage https://orcid.org/0000-0001-8611-9296
Houqiang Fu https://orcid.org/0000-0002-1125-8328

1) M. Higashiwaki, AAPPS Bull **32**, 3 (2022).
2) M. Hiroki, Y. Taniyasu, and K. Kumakura, IEEE Electron Device Lett. **43**, 350 (2022).
3) D. Araujo, M. Suzuki, F. Lloret, G. Alba, and P. Villar, Materials (Basel) **14**, 7081 (2021).

4) N. Izyumskaya, D. O. Demchenko, S. Das, Ü. Özgür, V. Avrutin, and H. Morkoç, Adv. Electron. Mater. **3**, 1600485 (2017).
5) R. J. Kaplar, A. A. Allerman, A. M. Armstrong, M. H. Crawford, J. R. Dickerson, A. J. Fischer, A. G. Baca, and E. A. Douglas, ECS J. Solid State Sci. Technol. **6**, Q3061 (2017).
6) J. L. Lyons, Semicond. Sci. Technol. **33**, 05LT02 (2018).
7) H. He, R. Orlando, M. A. Blanco, R. Pandey, E. Amzallag, I. Baraille, and M. Rérat, Phys. Rev. B **74**, 195123 (2006).
8) T. Gake, Y. Kumagai, and F. Oba, Phys. Rev. Materials **3**, 044603 (2019).
9) K. D. Chabak et al., , Semicond. Sci. Technol. **35**, 013002 (2020).
10) X. Ji, C. Lu, Z. Yan, L. Shan, X. Yan, J. Wang, J. Yue, X. Qi, Z. Liu, and W. Tang, J. Phys. D: Appl. Phys. **55**, 443002 (2022).
11) X. Lu, Y. X. Deng, Y. L. Pei, Z. M. Chen, and G. Wang, J. Semicond. **44**, 061802 (2023).
12) B. Zhang, J. Su, X. Guo, L. Zhou, Z. Lin, L. Feng, J. Zhang, J. Chang, and Y. Hao, Adv. Sci. **7**, 1903044 (2020).
13) Y. Kokubun, S. Kubo, and S. Nakagomi, Appl. Phys. Express **9**, 091101 (2016).
14) J.-S. Li, C.-C. Chiang, X. Xia, T. J. Yoo, F. Ren, H. Kim, and S. J. Pearton, Appl. Phys. Lett. **121**, 042105 (2022).
15) X. Lu, X. Zhou, H. Jiang, K. W. Ng, Z. Chen, Y. Pei, K. M. Lau, and G. Wang, IEEE Electron Device Lett. **41**, 449 (2020).
16) J. Zhang et al., Nat. Commun. **13**, 3900 (2022).
17) K. Sasaki, S. Yamakoshi, and A. Kuramata, Proc. SPIE **10919**, 1091913 (2019).
18) Q. Yan et al., Appl. Phys. Lett. **118**, 122102 (2021).
19) Y. Lv et al., IEEE Trans. Power Electron. **36**, 6179 (2021).
20) B. Wang, M. Xiao, J. Spencer, Y. Qin, K. Sasaki, M. J. Tadjer, and Y. Zhang, IEEE Electron Device Lett. **44**, 221 (2023).
21) Y. Wang, C. Wu, D. Guo, P. Li, S. Wang, A. Liu, C. Li, F. Wu, and W. Tang, ACS Appl. Electron. Mater. **2**, 2032 (2022).
22) P. Gopalan et al., Appl. Phys. Lett. **117**, 252103 (2020).
23) Z. Guo, A. Verma, X. Wu, F. Sun, A. Hickman, T. Masui, A. Kuramata, M. Higashiwaki, D. Jena, and T. Luo, Appl. Phys. Lett. **106**, 111909 (2015).
24) H. Fu, H. Chen, X. Huang, I. Baranowski, J. Montes, T.-H. Yang, and Y. Zhao, IEEE Trans. Electron Devices **65**, 3507 (2018).
25) K. Sasaki, A. Kuramata, T. Masui, E. G. Víllora, K. Shimamura, and S. Yamakoshi, Appl. Phys. Express **5**, 035502 (2012).
26) S. Jang, S. Jung, K. Beers, J. Yang, F. Ren, A. Kuramata, S. J. Pearton, K. H. Baik, and J. Alloys, Compd **731**, 118 (2018).
27) Y. Kim, M.-K. Kim, K. H. Baik, and S. Jang, ECS J. Solid State Sci. Technol. **11**, 045003 (2022).
28) A. Kuramata, K. Koshi, S. Watanabe, Y. Yamaoka, T. Masui, and S. Yamakoshi, Jpn. J. Appl. Phys. **55**, 1202A2 (2016).
29) W. Hao, Q. He, K. Zhou, G. Xu, W. Xiong, X. Zhou, G. Jian, C. Chen, X. Zhao, and S. Long, Appl. Phys. Lett. **118**, 043501 (2021).
30) S. M. Sze and K. K. Ng, *Physics of Semiconductor Devices* (Wiley, New Jersey, 2007) 3rd ed.
31) H. Gong, X. Chen, Y. Xu, Y. Chen, F. Ren, B. Liu, S. Gu, R. Zhang, and J. Ye, IEEE Trans. Electron Devices **67**, 3341 (2020).
32) Q. Yan, H. Gong, H. Zhou, J. Zhang, J. Ye, Z. Liu, C. Wang, X. Zheng, R. Zhang, and Y. Hao, Appl. Phys. Lett. **120**, 092106 (2022).
33) J.-S. Li, C.-C. Chiang, X. Xia, F. Ren, and S. J. Pearton, J. Vac. Sci. Technol. A **40**, 063407 (2022).